Published in final edited form as:

Adv Mater. ; : e73325. doi:10.1002/adma.73325.

A 3D-Printed Scaffolded Hydrogel Microneedle Array Biosensor for Real-Time, Continuous Monitoring

Jean Won Kwak,
Department of Radiology, Stanford University, Stanford, CA 94305, USA.

Tuan Trinh,
Department of Radiology, Stanford University, Stanford, CA 94305, USA.

Alexander D. White,
Department of Bioengineering, Stanford University, Stanford, CA 94305, USA.

Department of Electrical Engineering, Stanford University, Stanford, CA 94305, USA.

Yihang Chen,
Department of Radiology, Stanford University, Stanford, CA 94305, USA.

Department of Materials Science and Engineering, Stanford University, Stanford, CA 94305, USA.

Noah Eckman,
Department of Chemical Engineering, Stanford University, Stanford, CA 94305, USA.

Ishaan Jain,
Department of Radiology, Stanford University, Stanford, CA 94305, USA.

Yue Xu,
Department of Radiology, Stanford University, Stanford, CA 94305, USA.

Nghi Nguyen,
Department of Bioengineering, Stanford University, Stanford, CA 94305, USA.

Deepak Gopalan,
Department of Electrical Engineering, Stanford University, Stanford, CA 94305, USA.

Ye Eun Kim,
School of Chemical Engineering, Sungkyunkwan University (SKKU), Suwon 16419, Republic of Korea.

Netra Unni Kamat,
Department of Bioengineering, Stanford University, Stanford, CA 94305, USA.

John R. Tumbleston,

[*] jmdesimone@stanford.edu (J.M.D); tsoh@stanford.edu (H.T.S).
J. W. Kwak and T. Trinh contributed equally to this work.

Competing interests: JMD declares that he has an equity stake in Carbon Inc., which is a venture-backed start-up company that owns related U.S. Patent 9,216,546, U.S. Patent 9,360,757, and others. NUK, JRT, MTD, and JMD all have an equity stake in PinPrint, which is an early-stage vaccine and drug delivery company that has licensed MAP technology from Stanford, the University of North Carolina at Chapel Hill and Carbon. Methods for negative space preservation iCLIP are the subject of a pending patent application. The authors declare that they have no other competing interests.

Department of Radiology, Stanford University, Stanford, CA 94305, USA.

Chan Ho Park,
Department of Radiology, Stanford University, Stanford, CA 94305, USA.

Department of Chemical and Biological Engineering, Gachon University, Seongnam 13120, Republic of Korea.

Alex Yoshikawa,
Department of Radiology, Stanford University, Stanford, CA 94305, USA.

Jenny Ji,
Department of Bioengineering, Stanford University, Stanford, CA 94305, USA.

Maria Theresa Dulay,
Department of Radiology, Stanford University, Stanford, CA 94305, USA.

Michael Eisenstein,
Department of Radiology, Stanford University, Stanford, CA 94305, USA.

Eric A. Appel,
Department of Bioengineering, Stanford University, Stanford, CA 94305, USA.

Department of Materials Science and Engineering, Stanford University, Stanford, CA 94305, USA.

Jaeyun Kim,
School of Chemical Engineering, Sungkyunkwan University (SKKU), Suwon 16419, Republic of Korea.

Joseph M. DeSimone*,
Department of Radiology, Stanford University, Stanford, CA 94305, USA.

Department of Chemical Engineering, Stanford University, Stanford, CA 94305, USA.

Hyongsok Tom Soh*
Department of Radiology, Stanford University, Stanford, CA 94305, USA.

Department of Bioengineering, Stanford University, Stanford, CA 94305, USA.

Department of Electrical Engineering, Stanford University, Stanford, CA 94305, USA.

Abstract

Hydrogel-based biosensors offer a promising platform for designing microneedles capable of continuously tracking biomarkers in real time. However, such biosensors have been limited by the mechanical properties of hydrated hydrogels, which are generally ineffective at penetrating the skin to access interstitial fluid (ISF). As a solution, we have developed a microneedle-array biosensor (MAB) patch that enables continuous, reversible sensing by coupling fluorescent DNA aptamer switches to a hydrated hydrogel mesh within a 3D-printed scaffold. This scaffold provides essential mechanical support for skin insertion while preserving the apatmer-hydrogel's sensing functionality in the ISF. We demonstrate this design by tuning both aptamer switch design and hydrogel mesh size to detect exogenous levels of stress hormone cortisol and the metabolite adenosine triphosphate. We subsequently incorporated our cortisol-sensing hydrogel into the MAB scaffold and coupled this system to a custom-designed portable optical detector. Following *in*

vitro validation, we demonstrated the biocompatibility and *in vivo* utility of our system by conducting continuous, real-time measurements of exogenous cortisol in the ISF of live rats. These results demonstrate, for the first time, submicromolar detection using a sensor-embedded hydrogel microneedle system, highlighting the MAB platform as a versatile solution for real-time, continuous *in vivo* biosensing.

Keywords

molecular sensing; microneedle; additive manufacturing; aptamer; hydrogel

1. Introduction

Dermal interstitial fluid (ISF) is a blood filtrate that can be readily accessed beneath the skin surface to enable real-time monitoring of clinically-relevant biomarkers (1). Recent studies have demonstrated that continuous, real-time analysis of ISF can provide personalized health information (2), facilitate early disease detection (3), and support post-surgical care (4), thereby enabling timely and informed interventions. Continuous glucose monitors (CGMs) are a particularly successful example, enabling robust glycemic control for diabetic patients through ISF monitoring (5) and exemplifying the diagnostic utility of real-time, continuous biosensing. Unfortunately, existing CGM designs cannot be generalized beyond glucose analysis due to their reliance on a glucose oxidase-based detection mechanism that cannot be applied to other biomolecular analytes (6). This has necessitated the exploration of alternative platforms that can incorporate diverse recognition elements, such as aptamers or antibodies, in order to achieve broad applicability to other biomarkers.

Microneedle-array sensors have emerged as a particularly promising solution for continuous biomarker monitoring (3, 7–9). In particular, hydrogel-based microneedle-array sensors have demonstrated numerous advantages, including excellent biocompatibility at tissue interfaces, a three-dimensional meshed network for reagent loading, and ease of modification to optimize sensor architecture, functionality, and mechanical properties for different applications (10). These systems have been extensively applied in drug delivery, loaded with therapeutic agents (11–14) or in diagnostics, acting as matrices for ISF sampling (10, 15–17). However, when adapted as point-of-care sensing matrices, hydrogel-based microneedles necessitate two critical criteria: (i) providing a microenvironment that preserves the functionality of biorecognition elements, and (ii) possessing sufficient mechanical strength to penetrate skin. Simultaneously achieving these requirements presents a fundamental materials challenge. Densely crosslinked hydrogels offer the mechanical robustness needed for insertion but limit molecular accessibility (18). In contrast, loosely crosslinked hydrogels offer improved analyte diffusion and binding interactions (19), yet lack the stiffness necessary for effective skin insertion. To address this trade-off, current strategies often rely on drying processes to temporarily enhance mechanical strength (10, 15, 20) before skin insertion. However, such drying induces irreversible collapse of the hydrogel's porous polymer network (21), which is particularly problematic in systems employing reversible molecular switches that require a structurally stable microenvironment for reproducible function (19). As such, an alternative design strategy is needed to decouple the mechanical

and functional constraints of hydrogel-based microneedle sensors, enabling their application in continuous, *in situ* biomolecular monitoring.

In this work, we present a hydrogel-based microneedle system that couples aptamer switching to hydrogel confinement and incorporates a 3D printed scaffold to decouple the hydrogel's mechanical properties from its structural and sensing functions, enabling *in vivo* and *in situ* continuous molecular sensing at submicromolar levels. Our microneedle-array biosensor (MAB) patch incorporates an aptamer-hydrogel biosensing module that utilizes fluorescent DNA aptamer switches immobilized within a biocompatible poly(ethylene glycol) diacrylate (PEGDA)-based hydrogel. The aptamer switches generate a reversible fluorescent response upon target binding within the hydrogel mesh, enabling continuous measurements. The structural integrity of the soft aptamer-hydrogel module is preserved during and following skin penetration by housing it within a reinforcing scaffold fabricated by high-resolution Continuous Liquid Interface Production (CLIP) (22, 23), an additive manufacturing method that enables 3D printing at submicron scales (24, 25). We first developed an aptamer-hydrogel sensor for cortisol, a stress-related hormone, by tuning both our rationally-designed aptamer switches and the hydrogel mesh to achieve optimal sensor performance. We further demonstrate the potential generalizability of this aptamer-hydrogel design by producing a sensor for adenosine triphosphate (ATP) detection. We subsequently assembled a cortisol MAB and evaluated it in terms of skin penetration, aptamer retention, and optical blocking of skin autofluorescence. We also confirmed its cortisol-sensing performance *in vitro* using a custom-developed portable optical detector, achieving a limit of detection (LOD) of 500 nM. Finally, we demonstrate the *in vivo* utility of our MAB design by recording real-time, continuous cortisol levels in a live rat for four hours following a single cortisol (hydrocortisone) injection, replicating results obtained in previous studies of hydrocortisone pharmacokinetics. These results demonstrate that the MAB platform overcomes the mechanical limitations of soft hydrogels, offering a robust solution for real-time, *in situ* biomolecular monitoring within the ISF.

2. The MAB Platform

Our MAB platform enables continuous measurement of small-molecule analytes in dermal ISF using hydrogel-based sensors housed within mechanically robust, customizable CLIP-printed scaffolds (Figure 1A). The biosensing module consists of fluorescently-labeled DNA aptamer switches immobilized within a PEGDA-based hydrogel mesh. The aptamer switches themselves are rationally designed based on an intramolecular strand displacement (ISD) strategy (26), with their termini labeled with fluorophore and quencher groups, where the fluorophore group is also coupled to the hydrogel scaffold via acrydite-based chemical conjugation. The switches respond to target binding by undergoing a reversible conformational change, which separates the quencher and fluorophore groups and thus produces an optical signal. When the target unbinds from the aptamer switch, the fluorescence is once again quenched, enabling continuous real-time monitoring. The aptamer-hydrogel module enables 3D volumetric sensing, which produces a stronger signal relative to standard planar, surface-attached sensors while also protecting aptamers from direct interaction with tissues.

To enable robust *in situ* continuous biochemical monitoring upon skin penetration, our design leverages a CLIP-printed opaque scaffold that preserves the biosensing module's hydrated state while also offering physical support for the gel and mechanical strength for skin penetration. While existing hydrogel systems utilize drying to enhance mechanical stiffness for skin penetration, this process irreversibly collapses the hydrogel microenvironment (10, 15–17, 20), thereby disrupting aptamer conformational switching and preventing real-time, continuous sensing. Our design features function decoupling of skin penetration via CLIP print mechanical integrity and continuous monitoring of a hydrated biosensing module, where each microneedle-shaped CLIP scaffold serves as a structured void that houses and protects an aptamer-hydrogel biosensing module. Moreover, the opaque scaffold offers optical obstruction against tissue autofluorescence, with the side openings in the scaffold allowing the biosensing module to interface directly with ISF, such that small molecules can diffuse into the hydrogel. Collectively, as the target binds to these aptamer switches, the fluorescence signal increases, and the openings on the rear of the patch allow a portable optical detector (POD) to quantify the resulting signals through real-time ratiometric fluorescence measurements.

3. Design of the aptamer-based biosensing module

We rationally design the aptamer-based biosensing module for optimal binding and fluorescence-based signal transduction. Each ISD switch consists of a fluorescently-labeled target-binding aptamer connected to a quencher-modified intramolecular complementary displacement strand (DS) via a poly-T linker (Figure 1B) (19, 26). Upon target binding, the aptamer undergoes a conformational change, disrupting DS hybridization, leading to fluorophore-quencher separation and thereby generating an increase in fluorescent signal. This structure switching is governed by the competition between aptamer-binding (K_D^{apt}) and DS hybridization, which in turn informs the overall affinity (K_D) for the analyte. Increasing the length of DS hybridization or decreasing the poly-T length independently leads to an increase in K_D, which shifts the sensing dynamic range to higher target concentrations (26).

As an initial demonstration, we developed and optimized a biosensing module for the stress hormone cortisol. We first converted a previously-identified 67-nucleotide (nt) cortisol aptamer (K_D = 500 nM) (27) into a cortisol aptamer switch. To begin, we constructed two ISD switches with DS lengths of 9 or 10 nt and a 20-nt poly-T linker. We coupled the ISDs to a Cyanine3 (Cy3) dye label at the 5' end and an Iowa Black FQ quencher at the 3' end of the construct (see Table S1, Supporting Information, for all sequences used in this work). Using a standard plate-reader assay in buffer, we observed the expected change in fluorescence as a function of cortisol concentration. However, the aptamer switch with the 9-nt DS showed high background and suppressed switching, potentially due to weak DS hybridization (26). In contrast, the construct with the 10-nt DS exhibited robust binding-induced switching (Figure S1A, Supporting Information). We then modified this 10-nt DS construct to incorporate a variety of different poly-T linkers spanning 10, 20 or 30 nt (T10, T20, and T30, respectively), with an internal Cyanine5 (Cy5) dye coupled to an acrydite chemical handle at the 5' end and an Iowa Black RQ quencher at the 3' end. We again evaluated these switches in buffer across varying cortisol concentrations using a plate-reader assay. The T10 cortisol switch exhibited the lowest affinity (K_D = 3.3 μM)

with the highest signal gain (peak $F/F_0 = 3.58$), whereas the T30 cortisol switch had the highest cortisol affinity ($K_D = 412$ nM) but the lowest signal gain (peak $F/F_0 = 1.17$) due to increased background signal (Figure S1B, Supporting Information).

The ISD aptamer switches were in turn anchored to a hydrogel mesh network. Hydrogels provide considerable advantages as a sensor substrate by supporting three-dimensional volumetric sensing, which enhances optical signal strength (19) compared to 2D sensing materials. In addition, the hydrated hydrogel offers a uniform refractive index and a stable optical path for fluorescence measurements (28), enabling accurate and repeatable optical transduction. We chose PEGDA (average molecular weight ≈ 6,000 Da) for the hydrogel backbone because it met our criteria in terms of high tunability, biocompatibility, neutral charge, established utility in cell studies, and resistance to biofouling (19, 29, 30). We combined the acrydite-modified aptamer switches with PEGDA and a biocompatible photoinitiator (lithium phenyl-2,4,6-trimethylbenzoylphosphinate) in a buffer that mimics the physiological conditions of ISF (31, 32). We used ultraviolet (UV; 365 nm, 3.5 min) light to polymerize the aptamer-hydrogel precursor and form the biosensing module. We tuned the mesh size by varying the concentrations of PEGDA (10, 20, 40 w/v%), and calculated the resulting mesh size based on the swelling ratio and shear modulus of the hydrogels, and found that a higher concentration corresponded to a smaller mesh size (Figure S2, Supporting Information) (33, 34). To visualize the differences in morphology and internal structure, we also performed scanning electron microscopy (SEM) on lyophilized hydrogels (Figure 2A).

We first performed ultraviolet-visible (UV-Vis) spectroscopy to validate that aptamer-free hydrogels are insensitive to target introduction (Figure S3, Supporting Information). We observed minimal variation in absorbance intensity at 549 nm from hydrogels containing a Cy3-labeled anchor in the presence or absence of cortisol target, confirming that the observed signal differences arise from target-induced aptamer conformational changes rather than from swelling or bulk optical changes in the hydrogel.

We subsequently validated the immobilization of the aptamer switches within the hydrogel mesh for reliable *in situ* monitoring by performing washing steps before and after removing excess switches (Figure S4, Supporting Information) and by validating aptamer conjugation using the Fourier transform infrared (FTIR) spectroscopy (Figure S5, Supporting Information). We confirmed that the aptamer switches were properly conjugated within the mesh and remained embedded. While PEGDA dominates the FTIR spectrum as the bulk matrix, the aptamer-functionalized hydrogel exhibited modest intensity changes (including at the ester C=O band near ~1720 cm^{-1}) relative to PEGDA-only controls, consistent with formulation-dependent differences in the polymer environment.

For switching performance, we hypothesized that hydrogel mesh size would govern the behavior of immobilized aptamer switches, as the mesh provides sufficient steric space for conformational changes upon target binding. We evaluated the switching performance of the aptamer-hydrogel biosensing module. We prepared various hydrated aptamer-hydrogels in a standard 96-well plate, spiked in physiologically-relevant cortisol concentrations (0–100 μM) (35) in ISF buffer on top of each module, and observed the resulting fluorescence

change using a plate-reader. We tested the three ISD switches with a 10-nt DS and varying poly-T lengths under identical PEGDA concentrations (20 w/v%), and observed affinity trends that were consistent with those described above in buffer: T30 demonstrated the highest affinity, followed by T20 and T10 (Figure 2B).

We also examined the mechanical properties of the aptamer-hydrogel (20 w/v%, T20) in target-free and target-bound states using oscillatory shear measurements to assess whether target binding induces changes in viscoelastic behavior associated with bulk structural alterations (Figure S6, Supporting Information). Frequency sweeps (0.1–20 rad/s) showed gel-like properties across the tested frequency range, with the storage modulus (G') exceeding the loss modulus (G''). This suggests that the polymer network is well crosslinked and mechanically stable. In addition, the minimal differences in tan δ (G''/G') between hydrogels with and without the target confirm that target binding does not reorganize the polymer network. Therefore, the results show that the aptamer-hydrogel remains mechanically stable, confirming that sensing arises from molecular switching rather than material deformation.

When we evaluated switch performance in all three different hydrogel formulations, we found that both the switch length and hydrogel mesh size contributed to binding affinity (Figure 2C). An increase in the K_D was observed across all poly-T lengths when the aptamers were immobilized within the hydrogel mesh. Among the various lengths, T10—presumably due to its lower conformational flexibility—showed a more pronounced increase in K_D when immobilized in hydrogels. For the T20 and T30 switches, we observed notable changes in the 40 w/v% mesh, which resulted in a considerably higher K_D for both constructs. This is consistent with our hypothesis that a smaller hydrogel mesh creates steric hindrance that impedes the conformational change of larger aptamer switch constructs. We also assessed how the signal gain of the biosensing module was influenced by varying the mesh size while keeping the poly-T linker length constant. The T20 switch showed a higher signal gain in the 40 w/v% mesh (peak $F/F_0 = 2.01$) compared to 10 and 20 w/v% (peak $F/F_0 = 1.61$ and 1.83, respectively; Figure 2D). The T10 (Figure S7A, Supporting Information) and T30 switches (Figure S7B, Supporting Information) also demonstrated the same signal-gain trend as the T20 switch in the various meshes. These results highlight that a smaller mesh enhances signal gain, which is beneficial for *in situ* monitoring in terms of increasing signal intensity relative to background noise.

As a trade-off, this gain is offset by a slower temporal response in terms of molecular recognition (Figure 2E and Figure S8A, Supporting Information). After adding 5 μM cortisol solution on top of hydrogels coupled to the T20 switch, we observed the slowest kinetics leading to saturation in the 40 w/v% mesh compared to the 10 and 20 w/v% meshes. In order to rule out diffusion effects on sensor response, we performed experimental measurements of transport for the small-molecule dye fluorescein and observed no significant differences in diffusion kinetics across hydrogels of varying mesh sizes (Figure S8B, Supporting Information). Since the molecular weight of fluorescein (~0.8 nm in diameter; 332.31 g/mol) is comparable to that of cortisol (0.6–1 nm in diameter; 362.46 g/mol), we would expect similar diffusion behavior for the latter target. These results suggest that the observed differences in sensing kinetics primarily arise from changes in aptamer

switching behavior within the hydrogel, likely due to confinement or entanglement effects imposed by the mesh. In addition, it should be noted that we would anticipate a much faster response time from the MAB relative to this plate reader-based assay due to the smaller volume and size of each microneedle. This is because the time required for target diffusion through the hydrogel is proportional to the square of the hydrogel thickness and inversely proportional to the diffusivity (expressed as h^2/D, where h is thickness and D is diffusivity (36)).

To demonstrate the potential generalizability of our aptamer-hydrogel design, we constructed a biosensing module with ATP aptamer switches. We used an existing 37-nt ATP aptamer switch to generate an ISD construct with a 7-nt DS connected via T6, T16, and T26 poly-T linkers (26), and labeled with an internal Cy3 dye coupled to an acrydite chemical handle at the 5' end and an Iowa Black FQ quencher at the 3' end. As the ATP aptamer is shorter than the cortisol aptamer, these switches proved less susceptible to interference from the hydrogel mesh when undergoing conformational changes, with each construct exhibiting similar affinity across the three mesh sizes (Figure S9A, Supporting Information). As with the cortisol aptamer-hydrogel, we saw increased signal gain across all poly-T lengths as the hydrogel concentration increased (Figure S9B–D, Supporting Information). It is interesting to note that the ATP switches showed higher affinity within the 10 w/v% and 20 w/v% meshes than in buffer, contrary to our results with the cortisol switches.

These results are consistent with the relative length scales of the estimated aptamer switch sizes and hydrogel mesh sizes. Using polymer scaling laws in solution (37, 38), we can first estimate the size of the aptamer switches: $(r^2)^{1/2} \sim n^v \cdot l$, where $(r^2)^{1/2}$ represents the radius of gyration (*i.e.*, the effective size of the aptamer switch), n is the number of nucleotides, l is the monomer length (~0.34 nm per nucleotide, assuming flexible single-stranded DNA), and $v \approx 3/5$ for a self-avoiding random walk coil. The contour length of the fully-extended single-stranded DNA would be $n \cdot l$. Based on this scaling, the T10 and T30 cortisol aptamer switches (77 and 97 nt total length) have estimated size ranges of ~4.6–26.2 nm and ~5.3–33 nm, respectively. In comparison, the shorter ATP aptamer switches yield estimated size ranges of ~3.3–14.6 nm (for a T6 linker) and ~4.1–21.4 nm (for a T26 linker). The hydrogel mesh sizes are ~13.4 nm, ~12.1 nm, and ~11.0 nm for 10, 20, and 40 w/v% meshes, respectively (Figure S2C, Supporting Information). Comparing these length scales, when the size of the aptamer switch approaches the hydrogel mesh size, steric confinement may restrict its conformational freedom. For example, the T20 aptamer in the 40 w/v% hydrogel shows a higher effective K_D and slower switching kinetics compared to that in the 10 w/v% hydrogel, while also exhibiting enhanced fluorescence signal gain (F/F_0)—likely due to neighboring effects. In contrast, the relatively short ATP aptamer switches demonstrate enhanced binding with the structured mesh.

These observations and theoretical estimations demonstrate that our aptamer-hydrogel design enables spatial matching between the aptamer switches and the hydrogel mesh. This relationship is controlled by adjusting the poly-T linker length in aptamer switches and by varying the hydrogel mesh size through polymer concentration. Consequently, the effective KD can be tuned to the desired sensing range while achieving high F/F_0 optical signals,

with a trade-off in terms of temporal response. This optimization strategy is adaptable across different aptamer switch systems.

4. Design and characterization of the MAB scaffold

In conventional hydrogel microneedle arrays, a process of drying and subsequent rehydration and swelling is often used to improve skin penetration and promote interstitial fluid (ISF) uptake. This hydration-driven change alters scaffold porosity, which is favorable for drug release (11–14) or ISF sampling (10, 17), but can interfere with the reversible conformational switching of aptamers embedded within the hydrogel (21), preventing full recovery of their sensing function. Therefore, we conducted experiments to evaluate the necessity of using a pre-hydrated hydrogel for our aptamer-based sensing system. We performed drying-rehydration experiments to assess whether the biosensing module tolerates drying. We incubated the samples at 37 °C and 67 °C for 24 hours to fully remove residual water (12, 14, 39), followed by rehydration in ISF buffer for an hour. While native and dried-and-rehydrated aptamers immobilized on a surface (Fig. S10A, Supporting Information) show similar responses, the sensing hydrogel module exhibits a clear difference after drying, with the rehydrated module showing no detectable binding (Fig. S10B, Supporting Information). We also observed irreversible changes in the hydrogel structure (SEM images, Fig. S11, Supporting Information) along with noticeable changes in hydrogel volume upon rehydration (optical images, Fig. S12, Supporting Information). These results indicate that a fully-hydrated hydrogel is required to preserve aptamer function, necessitating the use of a separate structural scaffold to enable insertion into the skin.

We subsequently designed a 3D-printed methacrylate polymer-based scaffold structure for our MAB patch (Figure 3A–D; Figure S13, Supporting Information). The design objectives were to balance four key criteria: (i) matching the overall microneedle size, (ii) maximizing the hydrogel-housing void volume, (iii) ensuring sufficient mechanical strength (*i.e.,* strut thickness), and (iv) using an opaque material to reduce tissue autofluorescence. This scaffold provides sufficient mechanical integrity for reliable skin penetration, secure retention of the biosensing module, and minimal background interference from tissue autofluorescence *in situ* (40). At the same time, it preserves the aptamer-hydrogel module's capacity for molecular interactions in a natural, hydrated state while also providing physical protection and robust structural support. We have also demonstrated the flexibility of this design strategy with patches featuring microneedles of two different heights (Figure S14, Supporting Information).

We employed the S2 CLIP prototype printer developed by Carbon 3D, which has a pixel resolution of 5.4 μm and a build area of 8 mm × 14 mm, to generate our MAB scaffolds. The printer uses a 385-nm UV LED to initiate radical polymerization of a black methacrylate-based polymer (UMA 90) with a layer thickness of 10 μm using digital light processing. The MAB scaffold features a 5 × 5 array of four-strutted hollow microneedles with a needle-to-needle spacing of 1.25 mm, where each needle has a side triangular opening (height = 0.3 mm, base = 0.15 mm). Each microneedle is 1.65 mm long with an additional tapered pillar (height = 0.225 mm), meeting the design specification of penetrating the human dermis at a depth of 0.9–3.1 mm from the skin surface (41). The base of each needle is 0.5 × 0.5

mm^2, with the tapered pillar measuring 1 × 1 mm^2. The hollow interior of the microneedle structure extends down to the patch with an open back (0.35 × 0.35 mm^2), enabling the fluorescence signal from the biosensing module to be read using the POD. Finally, we dip-coated each scaffold with a biosensing module precursor solution (PEGDA 20 w/v% in ISF buffer) via capillary action, followed by UV photopolymerization (365 nm, LED) to fabricate the complete MAB patch (Figure 3B, C; see Figure S15, Supporting Information, for the step-by-step procedure and Figure S16, Supporting Information, for fluorescence images of the entire patch).

We used a standard compression setup (Instron) to compare the fracture forces of the MAB patch relative to a conventional solid hydrogel patch of identical dimensions and composition (Figure S17, Supporting Information). Successful skin penetration requires the fracture force of the patch to exceed the skin insertion force (0.058 N/needle) (42). The molded hydrogel patch (Figure 3E, gray) underwent compression without fracturing, with an almost negligible fracture force. In contrast, our MAB design with matching hydrogel composition (Figure 3E, red) exhibited compressive strength (~0.18 N/needle; total force = ~4.5 N), exceeding the reported skin puncture force without breaking. This indicates that the scaffold patch possesses sufficient mechanical strength for skin penetration, whereas the molded patch does not.

We then validated the mechanical integrity of our MAB patch by inserting it into excised porcine ear skin, which is compositionally similar to human skin (25, 43). After penetration, we examined the skin using optical coherence tomography (OCT) imaging and histological analysis with hematoxylin and eosin (H&E) staining (Figure 3F). These results showed that the MAB successfully penetrates the stratum corneum, the outermost skin layer, without damage to its interior structures. We also validated whether the scaffold provides structural protection to the biosensing module by measuring its fluorescence intensity via fluorescence microscopy through the back opening of the patch after repeated insertions and extractions into excised porcine ear skin. The results showed that the MAB retained its original fluorescence intensity (~95.7 %) after five insertions, confirming that the scaffold effectively preserves the integrity of the hydrogel (Figure S18, Supporting Information).

5. *In vitro* characterization of MAB-based biosensing

We subsequently evaluated the MAB platform's capacity for biosensing in a series of *in vitro* experiments. Within tissues, autofluorescent molecules such as keratin can increase the background signal, especially at wavelengths of 400–700 nm (40, 44). We therefore substituted the optical reporter Cy5 (excitation: ~640 nm) with a thermostable near-infrared (NIR) fluorophore, ATTO740, whose excitation wavelength (~740 nm) produces less autofluorescence and reduced light scattering within biological tissues (40). Based on the results from our aptamer-hydrogel design experiments from the previous section, we selected a 20 w/v% PEGDA hydrogel mesh due to its enhanced signal gain relative to the 10 w/v% hydrogel and faster kinetic response compared to the 40 w/v% hydrogel. Regarding the aptamer switch component, the T20 and T30 cortisol switches each exhibited performance trade-offs—T20 showed higher signal gain while T30 displayed higher binding affinity. To balance these properties, we constructed the T25 cortisol aptamer switch

with the ATTO740 fluorophore and Iowa Black RQ quencher (Figure S19, Supporting Information). When immobilized within the 20 w/v% hydrogel, this switch exhibited a K_D of 2.95 μM and an F/F_0 of 1.83, striking a good balance for these two important sensor parameters. In addition, we confirmed that the binding performance of the module remains comparable after UVC sterilization (Figure S20A, Supporting Information) and at body temperature (Figure S20B, Supporting Information). Furthermore, we demonstrated the feasibility of multi-day monitoring through *in vitro* experiments over a 3-day period, measuring fluorescence at Day 0 and Day 3 and observing no meaningful change in concentration-dependent response over this duration (Figure S20C, Supporting Information). We therefore selected this aptamer-hydrogel biosensing module for subsequent experiments.

For *in situ* monitoring purposes, we developed the NIR POD (25.4-mm diameter) to collect fluorescent signals from the MAB (Figure 4A; Figure S21, S22, Supporting Information). The detector features a far-red LED (740 nm) as the light source, with an excitation filter (707–763 nm) directing light to a 757-nm dichroic mirror. The mirror reflects excitation light to the MAB patch, which emits fluorescence at 764 nm from the ATTO740 reporter. An emission filter (728–890 nm) removes unwanted wavelengths before detection by a silicon photodetector. The signal is collected after processing via an Arduino circuit and amplified through a lock-in amplifier using a Python-based interface. In order to minimize photobleaching, the fluorescence signal is collected for 1.75 seconds, followed by a 5-second off period (Figure S23, Supporting Information). We validated our POD using the aptamer-hydrogel module consisted of the T25 cortisol switch in the 20 w/v% mesh. We collected fluorescence measurements at different cortisol concentrations in a black-walled 96-well plate (Figure S24, Supporting Information), and the resulting measurements correlated with those established by the T25 binding curve from our plate-reader assay (Figure S19, Supporting Information).

We first tested the fully-assembled MAB patch in a replicated physiological environment, using a synthetic skin phantom gel with an embedded microfluidic channel (1.8-mm diameter). This gel was composed of 1.4 wt% agarose in ISF buffer to replicate the optical and mechanical properties of skin (9) (Figure S25A, Supporting Information). We inserted the MAB patch into the gel and injected 500 nM cortisol through the channel. The fluorescence intensity reached 90% of the steady-state signal (F/F_0 = ~1.2) within 5 min (Figure 4B), demonstrating cortisol's diffusion kinetics from an artificial vein in a tissue-like environment. We next generated a binding curve for the MAB patch using a set of synthetic skin phantom gels with uniform cortisol concentrations (Figure S25B, Supporting Information). We chose this method over the channel-based one to ensure uniform target concentrations and avoid kinetic variability. We applied the MAB patch to each gel for 5 min and observed a corresponding increase in signal gain (F/F_0) as the cortisol concentration in the gel rose (Figure 4C). The signal gains of the MAB patch were slightly lower than those observed from the biosensing module in a 96-well plate. This may result from the difference in the total number of aptamer switches in each module, as the well contains a larger volume (~20 μL) than the MAB patch (< 0.1 μL/needle).

We then used the same phantom gel setup to evaluate continuous fluorescence response to varying target concentrations. We sequentially inserted the MAB patch into phantom gels

with different cortisol concentrations (0 nM, 500 nM, 1 μM, and 10 μM), with entailed washing with buffer prior to insertion into a cortisol-free gel (Figure 4D). The MAB patch exhibited concentration-dependent signals that were consistent with the measurements from our calibration curve, with a fluorescence change of approximately 1.15 for 500 nM, 1.3 for 1 μM, and 1.4 for 10 μM cortisol. Furthermore, to assess the long-term stability of our sensor, we performed continuous fluorescence measurement with our MAB in the cortisol-free phantom gel over the course of 90 min, and observed minimal photobleaching (Figure S26, Supporting Information).

Finally, we performed cytotoxicity studies with cultured human dermal fibroblasts (HDFs) to evaluate the biocompatibility of the MAB patch (Figure S27, Supporting Information). We immersed our cortisol MAB patches in the presence of HDFs (9) suspended in culture medium, with HDFs alone as a positive control, and used an acridine orange and propidium iodide stain assay to evaluated the ratio of live cells to dead cells. These viability assays revealed that HDFs cultured with MABs exhibited similar viability (95.6 ± 1.4 % and 92.1 ± 8.6 %) to the positive control (95.7 ± 3.8% and 96.9 ± 1.0 %) at 1 day and 5 days, respectively, after onset of MAB exposure. These results suggest the MAB patches are not toxic and are suitable for *in vivo* applications.

6. *In vivo* real-time, continuous cortisol measurements in rats

To confirm the feasibility of *in vivo* measurements with the MAB system, we first ensured that our 3D-printed scaffold was capable of minimizing background associated with autofluorescence from the skin. After confirming the optical blocking capability of the scaffold material via UV–Vis spectroscopy (Figure S28A, Supporting Information), we used the POD to measure the fluorescence intensity from shaved rat skin alone or after the insertion of either a bare MAB scaffold or a fully-assembled MAB patch. The fluorescence intensity of both the bare scaffold and the complete MAB patch was lower than that of the skin alone (Figure S28B, Supporting Information). This confirms that our optically-opaque patch design can effectively suppress environmental fluorescence (~50% reduction) during *in vivo* measurements.

We subsequently performed a series of experiments in three live rats to test the cortisol MAB's real-time continuous monitoring performance *in vivo*. Rats do not produce endogenous cortisol due to the absence of the necessary steroidogenic enzyme, and so we instead tracked the pharmacokinetics of exogenously administered hydrocortisone (synthetic cortisol) in the ISF for these experiments (45). We confirmed that the T25 cortisol switch from our aptamer-hydrogel component is not cross-reactive with corticosterone, the primary glucocorticoid produced by rats, indicating that this biomolecule should not interfere with our experiment (Figure S29A, Supporting Information). Furthermore, we confirmed that the biosensing module exhibits a similar response in filtered human serum (Figure S29B, Supporting Information); however, we did observe higher variability at elevated concentrations in serum compared to ISF, which may arise from factors including binding of free cortisol to globulin and albumin in plasma.

After inserting the MAB patch into the lower back of anesthetized rats, we aligned the POD on top of the patch (Figure 5A). To ensure the specificity of cortisol detection, we first administered saline via retro-orbital (R.O.) injection to examine the response and observed minimal change in signal (Figure 5B). We then administered 2.3 mg/kg synthetic cortisol (hydrocortisone) via the R.O. route to achieve cortisol levels comparable to those reported in hydrocortisone pharmacokinetics studies (35, 46, 47), and recorded the sensor signal for several hours. Based on an estimated rat blood volume of 64 mL/kg (48), this dosage corresponds to a blood concentration of approximately 36 μg/mL. As a representative trace from a single rat, we observed that the fluorescence signal of the MAB peaked (F/F_0 = 1.35) at 35 min post-administration, yielding a signal equivalent to an ISF cortisol concentration of 3.6 μg/mL (Figure 5C). Across rats (n = 3), the peak response (F_{max}/F_0) was 1.34 ± 0.06 and the time-to-peak was 61.6 ± 27.5 min post-administration (Figure S30, Supporting Information), with values reported as mean ± s.d. The differences in response across the three animals may be attributable to individual metabolic variability, absorption differences, or physiological factors (49). These results are consistent with previous studies, which found that the concentration of free cortisol in ISF is approximately 10% of the total cortisol level in blood (50).

Finally, we assessed the mechanical integrity of the MAB patch and skin condition before and after *in vivo* implantation. The MAB remained intact based on visual assessment (Figure S31A, Supporting Information), and the calibration curves were unchanged after the *in vivo* experiment (Figure S31B, Supporting Information). The skin at the insertion site showed puncture sites but no further observable skin damage (Figure S32, S33, Supporting Information), indicating minimal irritation by the MAB patch. These results showcase the feasibility of using the MAB system *in vivo* for the continuous monitoring of small analytes. Compared to reported hydrogel-based microneedles (Table S2, Supporting Information), our MAB system can monitor cortisol levels at submicromolar levels continuously, *in situ* upon a single bolus of cortisol injection, through the 3D-printed scaffold that facilitates skin penetration, and enables direct interfacing with dermal ISF while protecting the fragile biosensing module for extended continuous operation.

7. Conclusion

Our MAB system, which consists of a hydrogel-coupled fluorescent aptamer-based biosensing module housed within a reinforced 3D-printed scaffold, offers a robust platform for the real-time continuous monitoring of small-molecule analytes in ISF. Specifically, our aptamer-hydrogel design establishes a materials framework in which aptamer conformational dynamics are coupled to hydrogel network architecture, thereby governing binding affinity, signal gain, and response kinetics. This behavior arises not from simple integration but from a coupled materials system that establishes hydrogel confinement as a design parameter linking hydrogel mesh properties to aptamer switching behavior. With this design, one can tailor the aptamer switch design and hydrogel mesh size to achieve the desired binding performance (*e.g.* kinetics or affinity range) for a given target analyte. And by using a NIR fluorophore-based readout, we have demonstrated that the MAB system is compatible with use in live animals and retains the capacity for submicromolar target detection in real-time over extended periods. This platform

could theoretically be generalized for the monitoring of a wide range of metabolites and therapeutic agents by selecting or designing the appropriate aptamer switches and by employing different hydrogel materials and alternative biosensing modules (*e.g.*, antibody switches (51)). This will involve some additional effort in terms of optimizing switches to achieve high sensitivity, specificity, and kinetic response, as well as aligning the hydrogel mesh size with the target analyte dimensions. In addition, future work will integrate advanced adhesives and the flexible structures enabled by CLIP printing to improve conformal skin contact, long-term adhesion, biocompatibility, reusability, and user comfort, as well as incorporate clinical sterilization methods, thereby enhancing the device's suitability for translational studies. Advancements in electronics will focus on achieving a high signal-to-noise ratio and integrating the system into a wearable system with wireless data transmission to further facilitate long-term biomolecule monitoring in clinical settings and elsewhere.

8. Materials and Methods

Animal models:

All animal studies were performed in accordance with guidelines from Stanford's Institutional Animal Care and Use Committee (IACUC) and the Administrative Panel on Laboratory Animal Care (APLAC). *Ex vivo* porcine skin was sourced from freshly euthanized Yorkshire pigs (Pork Power), as per tissue harvest protocol (APLAC #34366). *In vivo* rat experiments were completed on 8- and 12-week old female Sprague Dawley rats (250–350g; Charles River Laboratories) (APLAC #33900).

Materials and reagents:

All chemicals were purchased from MilliporeSigma unless otherwise noted. Oligonucleotides modified with acrydite, amino group, Cy3, Cy5, or Iowa Black were purified via high-performance liquid chromatography (HPLC) and purchased from Integrated DNA Technologies (sequences in Table S1, Supporting Information). All oligonucleotides were resuspended in nuclease-free water and stored at −20 °C. ISF buffer consisted of 120 mM NaCl, 1 mM $MgCl_2$, 5 mM KCl, 1 mM $CaCl_2$, 20 mM Tris-HCl, and 0.01% Tween 20 in DI water (pH 7.5) (31). For MAB experiments, Tween 20 was removed. All experiments were repeated at least three times. Data are shown as mean ± SD ($n \geq 3$) and were analyzed with GraphPad Prism 10 software.

Measurement of binding affinity:

A Synergy H1 microplate reader (BioTek) was used to measure fluorescence spectra for optical aptamer switches in 96-well half-area black flat-bottom polystyrene microplates (Corning). Cy3-labeled ATP switch strands were assessed using a Cy3 filter cube (Semrock; 540/25 nm excitation, 590/35 nm emission), while Cy5-labeled cortisol switch strands were analyzed with a Cy5 filter cube (620/40 nm excitation, 680/30 nm emission). For NIR cortisol switches, a strand with an internal amino modifier was conjugated with ATTO 740 (NHS-ester, ATTO-TEC) and subsequently purified via HPLC. NIR fluorescence measurements were performed using a Spark microplate reader (Tecan Life Sciences) with 745/20 nm excitation and 790/25 nm emission.

For aptamer switches in buffer, binding affinity studies were conducted by suspending 500 nM aptamer in ISF buffer. Each well of the 96-well half-area plate contained 40 μL of solution with a final concentration of 250 nM aptamer and various final target concentrations. For cortisol measurements, a 30 mM cortisol stock solution in 100% ethanol was used for serial dilution to achieve concentrations ranging from 0 to 100 μM in ISF buffer. For ATP, target concentrations ranged from 0 to 10 mM ATP, prepared by serial dilution of a 100 mM ATP stock solution (ThermoFisher) in ISF buffer.

For the aptamer-hydrogel, the precursor was created by mixing PEGDA (MW ≈ 6,000 Da) at different final concentrations (10, 20, 40 w/v%), 0.1 w/v% lithium phenyl-2,4,6-trimethylbenzoylphosphinate (LAP), and acrydite-functionalized oligonucleotides at a final concentration of 250 nM in ISF buffer. Each well of the 96-well plate contained 20 μL of this precursor mix, which was then subjected to UV curing (Opticure APM LED CUBE II, 365 nm, 3.5 min) for polymerization. Each well was rinsed with ISF buffer to remove excess unbound aptamers. 20 μL of target in ISF buffer was then added on top and allowed to diffuse into the aptamer-hydrogel. We evaluated binding affinity with final concentrations of 0–100 μM cortisol or 0–10 mM ATP in ISF buffer. For the human serum experiment, pooled human serum (MP Biomedicals) was filtered using an Amicon centrifugal filter (Amicon Ultra, 100 kDa MWCO) to mimic ISF.

To evaluate the impact of drying and rehydration on aptamer functionality, biotin-labeled cortisol aptamers were immobilized onto streptavidin-coated 96-well plates (Thermo Fisher). For the native condition, wells were maintained in ISF buffer. For the dried-and-rehydrated condition, the plates were dried at 37 °C for 24 hours and then rehydrated with ISF buffer containing serially-diluted cortisol at a range of concentrations prior to measurement. For the impact of drying and rehydration on aptamer-hydrogel functionality, cortisol aptamer-hydrogels (20 w/v%) were prepared in 96-well half-area microplates following the fabrication protocol described above. For the drying condition, fully polymerized hydrogels were dried in an oven at 37 °C for 24 hours and subsequently rehydrated in ISF buffer for 1 hour prior to testing with serial cortisol concentrations. For the UVC sterilization test, polymerized aptamer-hydrogels within the microplates were sterilized using a UV light sanitizer (Knizen) for 3 minutes. To mimic skin physiological conditions, plate-reader measurements were conducted at 34 °C to evaluate aptamer-hydrogel performance at this temperature. For extended *in vitro* testing, the cortisol aptamer-hydrogels in microplates with target solutions were sealed with adhesive PCR plate seals (Thermo Fisher) to prevent evaporation and stored at room temperature. Binding affinity was evaluated at Day 0 and Day 3.

Analysis of binding properties:

Representative concentration-dependent emission spectra for both ATP and cortisol aptamers were fitted to the Langmuir isotherm binding model, with emission (F) versus [target] for each aptamer strand:

$$F = A\frac{[target]}{K_D + [target]} + y_0$$

(1)

where K_D is the dissociation constant, A is the magnitude of the binding response, and y_0 is the background signal at zero target concentration. To account for minor variations in aptamer concentration between samples, binding curves were normalized to a range of 0 to 1 to emphasize changes in affinity. For fluorescence measurements, binding curves were expressed as $F = F/F_0$, where F_0 represents the average baseline fluorescence signal. Error bars represent the standard deviation of fluorescence measurements from three replicates.

Material characterization of the aptamer-hydrogel module and scaffold:

The hydrogel mesh sizes were assessed using the equation $\xi \approx l\sqrt{RTC_n\rho/xM_rGQ}$ (33), incorporating both empirical and experimental data. Here, l represents the monomer size (typically 1.54 nm), and the characteristic constant (C_n) is 4 for PEG. The density (ρ) of PEGDA is 1,006.25 kg/m^3, and x is a network-type factor set to 2 due to the presence of two chains. M_r, the molar mass, is 0.055 kg/mol for the PEG monomer. Two variables—elastic modulus (G) and mass swelling ratio (Q)—were experimentally determined using hydrogel disks. Elastic modulus was evaluated via frequency sweep using a TA DHR-2 rheometer between 0.1 and 100 s^{-1}, and the swelling ratio was calculated as the final mass divided by the initial mass obtained by immersing the hydrogel in ISF buffer overnight.

UV–Vis spectra were collected using a spectrometer (Agilent Cary 6000i) over the wavelength range of 350–700 nm for the aptamer-hydrogel at room temperature. Hydrogel precursor solutions (20 w/v%) with or without Cy3-labeled anchor strands were loaded into cuvettes (Azzota Corp) and polymerized by UV curing (Opticure APM LED CUBE II, 365 nm) for 3.5 min. Then, ISF buffer with or without cortisol (100 μM), was added on top of the hydrogels and incubated overnight prior to UV–Vis measurements. For the scaffold material (UMA 90 Black, Carbon; thickness = 0.2 mm), UV–Vis spectra were recorded over the wavelength range of 200–1500 nm at room temperature, with the control measurement performed in the absence of the material.

To evaluate the immobilization percentage of switches on hydrogel meshes (PEGDA 6k, 20 w/v%), a washing experiment was conducted using aptamer-hydrogel samples in 96-well half-area black flat-bottom plates. Each well contained 20 μL of the aptamer-hydrogel precursor. The 'not immobilized' group was not photopolymerized, while the 'immobilized' group underwent photopolymerization as described above. Fluorescence measurements were taken before and after three washes with ISF buffer using a Spark microplate reader.

Fourier transform infrared (FTIR) spectroscopy was performed using a Nicolet iS50 FTIR spectrometer equipped with an attenuated total reflectance (ATR) accessory to characterize the chemical composition of PEGDA and aptamer-functionalized PEGDA hydrogels. Spectra of dried hydrogel samples (10 × 5 × 2 mm^3) were collected over the range of 3300–700 cm^{-1}, and all spectra were baseline-corrected prior to analysis.

Rheological measurements were performed using a TA Instruments DHR-2 rheometer equipped with a parallel plate geometry (8 mm diameter) at room temperature. Aptamer-hydrogel disks (50 μL; ~9 mm diameter, ~1 mm height) were allowed to swell overnight

in ISF buffer with or without cortisol prior to measurement. The storage modulus (G') and loss modulus (G'') were evaluated by frequency sweeps over an angular frequency range of 0.1–20 rad/s at a fixed strain (0.5%), and by amplitude sweeps over a strain range of 0.1–10% at a fixed angular frequency (1 rad/s).

Diffusion kinetics in the aptamer-hydrogel modules were evaluated using hydrogel disks (20 μL; ~4.8 mm diameter, ~1.1 mm height) prepared as described above and placed in 96-well half-area black flat-bottom plate. 20 μL target solution in ISF was added on top of the aptamer-hydrogel, and emission measurements were taken at 10-second intervals using a Synergy H1 microplate reader (BioTek). For hydrogel diffusion and release kinetics, we used fluorescein (0.5 mg/mL; 332.31 g/mol). Hydrogel disks (10 μL; ~4.8 mm diameter, ~0.5 mm height) were fully hydrated and incubated with 0.5 mg/mL fluorescein overnight. Following incubation, hydrogels were transferred to fresh ISF buffer, and fluorescein release was quantified at 1, 2, 3, and 24 hours. At each time point, the buffer was removed, and fluorescence was measured using a plate reader (488 nm excitation /510 nm emission). The sample was then placed in fresh buffer.

Fabrication of the complete MAB assembly:

We designed our scaffolds using computer-aided design software (Solidworks, nTopology). Each microneedle measures ~1,300–1,650 μm in height, with a base size of 0.5 mm. The filleted pillar connecting the microneedle and its base is 0.225 mm in height. The opening in the back is 0.35 mm by 0.35 mm, while the center-to-center spacing between the microneedles is 1.25 mm (Figure S6, Supporting Information). We used the prototype high-resolution CLIP printer (S2, Carbon) to 3D print MAB scaffolds in UMA 90 (Black, Carbon) with 10 μm slice thickness. The cleaning procedure included sonication in an isopropyl alcohol bath and UV curing (Opticure APM LED CUBE II, 365 nm, 5 min), followed by autoclaving. Plasma treatment (Harrick Plasma, 45W, O_2 22 sccm, 15 min) increased surface hydrophilicity on the MAB scaffolds. We then dip-coated the scaffold with aptamer-hydrogel precursor (2 μM T25 cortisol aptamer switch, PEGDA 20 w/v%) to enable the filling of voids within the plasma-treated scaffolds via capillary action. The UV oven was used to polymerize the aptamer-hydrogel inside the scaffold. The MAB was rinsed three times with ISF buffer to remove any unreacted residues and then stored in ISF buffer at 4 °C until use.

Imaging of hydrogels and MABs:

A scanning electron microscope (SEM; Apreo S LoVac SEM, Thermo Fisher Scientific) was used to image both the hydrogel microstructures and the microneedle geometry. We prepared three hydrogel conditions: native (never-dried) hydrogels and hydrogels oven-dried at 37 °C or 67 °C for 24 hours, followed by rehydration in ISF buffer for an hour. An Olympus DSX1000 microscope (Evident Scientific) was used to measure the geometries of aptamer-hydrogels and MABs. For visualization, we prepared ~1 mm-thick aptamer hydrogels and sectioned them using a 2 mm biopsy punch (Miltex). Native hydrogels were stored at 4 °C, whereas oven-dried hydrogels were rehydrated and prepared following the same procedure prior to imaging. Fluorescence microscopy (Olympus IX73) was used to

capture fluorescence in MABs and aptamer-hydrogels labeled with Cy3 and Cy5, using corresponding Cy3 and Cy5 filter cube sets (Edmund).

Mechanical characterization of MABs:

Force-displacement measurements were performed using the Instron 5565 Universal Testing Machine with a 5 kN load cell. For compression testing to determine fracture force, the MAB was mounted on the rigid base platform with the needles oriented upward, while the compression plate was lowered at a constant rate of 1 mm/min. Traditional microneedle patches of hydrogel (PEGDA 6k, 20 w/v%) were molded in a PDMS-based mold generated from an S2-printed master mold (Carbon).

MAB penetration in ex vivo porcine skin:

MABs were applied to thawed porcine ear skin, which was secured to a foam board. An MPatch Micro Applicator (Micropoint Technologies) delivered instantaneous vertical force to the MABs on the skin layer. Thumb pressure was applied for 10 seconds to enhance adhesion, followed by the application of a Tegaderm layer (3M) to secure the MABs in place. The skin samples with the attached MABs were fixed in 10% formalin overnight and subsequently transferred to 70% ethanol. 3D optical coherence tomography (OCT) (Ganymede SD-OCT, ThorLabs) was used to scan the puncture sites. Staff at the Histo-Tec Lab (Hayward, CA) performed paraffin embedding, sectioning, and hematoxylin and eosin (H&E) staining according to standard protocols.

Assembly of the portable optical detector (POD):

A schematic diagram of the POD is shown in Figure S13, Supporting Information, Standard Ø1” lens tubes (Thorlabs) formed the basis of the fluorescence detector. The “L”-shaped alignment included bi-convex lenses (Ø1”, N-BK7, Thorlabs) for focusing, an LED (XPEBFR-L1-0000-00801, Cree LED) mounted on a printed circuit board, and an excitation filter (735/28, Ø25 mm, Semrock). A dichroic mirror (FF757-Di01-25×36, Ø25 mm, Semrock) was positioned centrally, followed by an emission filter (809/81, Ø25 mm, Semrock) and a silicon photodetector module (200–1,100 nm; PDA100A2, Thorlabs) equipped with an embedded transimpedance amplifier to convert photocurrents to voltages. The LED was controlled by an Arduino board (Nano Every), powered at 5 V using a power supply (E3610A, Hewlett Packard). The light signal was amplified by a lock-in amplifier (SR830, Stanford Research Systems; sensitivity: 100 μV) before being routed to an Arduino board with an embedded microcontroller (ATMega4809, Microchip Technology). The processed signals were then transferred to a PC with a Python-based user interface for data acquisition.

Signal processing for the POD:

Fluorescence signals were collected by the POD, which operates an LED with a 1 kHz square wave in order to eliminate light leak contamination. The LED was switched on for 1.75 seconds to collect 10 data-points, followed by a 5-second off period before repeating. MATLAB code enabled data extraction at a sampling frequency of 0.148 Hz by averaging data-points and attenuating noise through a Savitzky-Golay filter. Signal from a bare MAB

scaffold was measured and averaged for use as a background value. This background value was subtracted from the data collected using the MAB patch with the aptamer-hydrogel. Signal processing is shown in Figure S15 (Supporting Information).

In vitro characterization of the MAB system:

For experiments using the POD, biosensing modules were prepared as hydrogel disks (20 μL) as described above and placed in 96-well half-area black flat-bottom polystyrene microplates. A 20 μL target solution was added on top of the aptamer-hydrogel. In subsequent models, a tube (inner diameter: 0.04”, outer diameter: 0.07”) was embedded in a skin phantom gel using a 3D-printed chamber. Two additional tubes, functioning as the inlet and outlet, allowed for the flow of simulated ISF containing cortisol through the phantom gel (Figure S17A, Supporting Information). The gel-based skin phantom gels comprised 1.4 wt% agarose (Invitrogen) with simulated ISF (BZ254, Biochemazone) to replicate the *in vivo* conditions of the dermal layer. Agarose gels with various concentrations of cortisol were prepared in a 24-well plate (Figure S17B, Supporting Information). Binding affinity, binding kinetics, and photobleaching were evaluated by inserting MABs into the phantom gels and continuously recording fluorescence (pausing interrogation during MAB transfer) using the POD. To revert to baseline, each MAB patch was washed once with ISF buffer to accelerate the target removal and then inserted into target-free gel.

Cell viability with in vitro human dermal fibroblasts (HDF):

HDF cells (9) (ATCC) were prepared with Dulbecco's Modified Eagle Medium (Thermo Fisher Scientific) with 10% fetal bovine serum (Thermo Fisher Scientific). The MAB patches were incubated with suspended cells in a 48-well plate at 37 °C with 5% CO_2 (Thermo Fisher Scientific). The positive control did not have MABs. At Day 1 and Day 5, cells were collected by trypsinization. Acridine orange and propidium iodide stain assays (Logos Biosystems, Luna automated cell counter) were used to determine cell viability.

In vivo rat experiments:

Experimental procedures with rat models followed protocols approved by the IACUC at Stanford University (protocol #33900). Three female rats (250–350g, Charles River Laboratories) were anesthetized with isoflurane (3–5% induction and 2.5% maintenance) and shaved on their backs, followed by a 1-minute application of Nair depilatory cream (Church and Dwight). Before patch application, the skin was sterilized using betadine and alcohol swabs. MABs were sterilized via UVC (UV light sanitizer, Knizen) for 3 min. An MPatch Micro Applicator was used to insert the MABs into rat skin, followed by thumb pressure to secure them. Once the patches were fixed, a layer of Tegaderm was applied. For real-time, continuous measurements, the POD was positioned parallel to and on top of the MAB, next to the anesthetized rat. After a 10-minute baseline collection, either saline (150 μL) or 2.3 mg/kg (150 μL) of USP-grade hydrocortisone (Solu-Cortef, Pfizer) was administered retro-orbitally (R.O.). Measurements were recorded for up to four hours before terminating the experiment. Once the measurements were completed, we immediately removed the patch, imaged the skin, and dissected and fixed the skin in 10% formalin overnight for H&E staining.

Supplementary Material

Refer to Web version on PubMed Central for supplementary material.

Acknowledgments

Part of this work was performed at nano@stanford RRID:SCR_026695. H.T.S. would like to acknowledge that research reported in this work was supported by the Leona M. and Harry B. Helmsley Charitable Trust and Wellcome LEAP SAVE program. J.W.K. gratefully acknowledges that research reported in this work was supported by the National Institute of Biomedical Imaging and Bioengineering of the National Institutes of Health under grant number K99EB036582. The content is solely the responsibility of the authors and does not necessarily represent the official views of the National Institutes of Health.

Data Availability Statement

All data are available in the main text or the Supplementary Materials.

References

1. Friedel M et al. , Opportunities and challenges in the diagnostic utility of dermal interstitial fluid. Nat Biomed Eng 7, 1541–1555 (2023). [PubMed: 36658344]
2. Kim J, Campbell AS, de Ávila BE, Wang J, Wearable biosensors for healthcare monitoring. Nat Biotechnol 37, 389–406 (2019). [PubMed: 30804534]
3. Zargartalebi H et al. , Active-reset protein sensors enable continuous in vivo monitoring of inflammation. Science 386, 1146–1153 (2024). [PubMed: 39636994]
4. Heikenfeld J et al. , Accessing analytes in biofluids for peripheral biochemical monitoring. Nat Biotechnol 37, 407–419 (2019). [PubMed: 30804536]
5. Chmayssem A et al. , Insight into continuous glucose monitoring: from medical basics to commercialized devices. Mikrochim Acta 190, 177 (2023). [PubMed: 37022500]
6. Flynn CD et al. , Biomolecular sensors for advanced physiological monitoring. Nat Rev Bioeng, 1–16 (2023).
7. Tehrani F et al. , An integrated wearable microneedle array for the continuous monitoring of multiple biomarkers in interstitial fluid. Nat Biomed Eng 6, 1214–1224 (2022). [PubMed: 35534575]
8. Wang Z et al. , Microneedle patch for the ultrasensitive quantification of protein biomarkers in interstitial fluid. Nat Biomed Eng 5, 64–76 (2021). [PubMed: 33483710]
9. Lin S et al. , Wearable microneedle-based electrochemical aptamer biosensing for precision dosing of drugs with narrow therapeutic windows. Sci Adv 8, eabq4539 (2022). [PubMed: 36149955]
10. Aroche AF, Nissan HE, Daniele MA, Hydrogel-Forming Microneedles and Applications in Interstitial Fluid Diagnostic Devices. Adv Healthc Mater 14, e2401782 (2025). [PubMed: 39558769]
11. Than A et al. , Self-implantable double-layered micro-drug-reservoirs for efficient and controlled ocular drug delivery. Nat Commun 9, 4433 (2018). [PubMed: 30401883]
12. Lee JW, Park J-H, Prausnitz MR, Dissolving microneedles for transdermal drug delivery. Biomaterials 29, 2113–2124 (2008). [PubMed: 18261792]
13. Caffarel-Salvador E et al. , A microneedle platform for buccal macromolecule delivery. Sci Adv 7, (2021).
14. Xu J et al. , Microneedle Patch-Mediated Treatment of Bacterial Biofilms. ACS Applied Materials & Interfaces 11, 14640–14646 (2019). [PubMed: 30933463]
15. Zheng M et al. , Osmosis-Powered Hydrogel Microneedles for Microliters of Skin Interstitial Fluid Extraction within Minutes. Adv Healthc Mater 9, e1901683 (2020). [PubMed: 32351042]
16. Bakhshandeh F et al. , Wearable Aptalyzer Integrates Microneedle and Electrochemical Sensing for In Vivo Monitoring of Glucose and Lactate in Live Animals. Adv Mater 36, e2313743 (2024). [PubMed: 38752744]

17. GhavamiNejad A et al. , Continuous insulin monitoring using an antibody-protecting zwitterionic microneedle patch. Nat Biomed Eng, (2025).
18. Behnam V et al. , mPatch: A Wearable Hydrogel Microneedle Patch for In Vivo Optical Sensing of Calcium. Angew Chem Int Ed Engl 64, e202414871 (2025). [PubMed: 39625999]
19. Park CH et al. , Real-Time Spatiotemporal Measurement of Extracellular Signaling Molecules Using an Aptamer Switch-Conjugated Hydrogel Matrix. Adv Mater 36, e2306704 (2024). [PubMed: 37947789]
20. Zheng H et al. , Hydrogel Microneedle-Assisted Assay Integrating Aptamer Probes and Fluorescence Detection for Reagentless Biomarker Quantification. ACS Sens 7, 2387–2399 (2022). [PubMed: 35866892]
21. Xu D et al. , Dehydration regulates structural reorganization of dynamic hydrogels. Nat Commun 15, 6886 (2024). [PubMed: 39128898]
22. Hsiao K et al. , Single-digit-micrometer-resolution continuous liquid interface production. Sci Adv 8, eabq2846 (2022). [PubMed: 36383664]
23. Kronenfeld JM, Rother L, Saccone MA, Dulay MT, DeSimone JM, Roll-to-roll, high-resolution 3D printing of shape-specific particles. Nature 627, 306–312 (2024). [PubMed: 38480965]
24. Rajesh NU et al. , 3D-Printed Microarray Patches for Transdermal Applications. JACS Au 2, 2426–2445 (2022). [PubMed: 36465529]
25. Rajesh NU, Jihyun (Luna) Hwang YX, Saccone Max A., Hung Andy H., Hernandez Rosa A.S., Coates Ian A., Driskill Madison M., Dulay Maria T., Jacobson Gunilla B., Tian Shaomin, Perry Jillian L., DeSimone Joseph M., Ed. (Advanced Materials, 2024).
26. Wilson BD, Hariri AA, Thompson IAP, Eisenstein M, Soh HT, Independent control of the thermodynamic and kinetic properties of aptamer switches. Nat Commun 10, 5079 (2019). [PubMed: 31699984]
27. Wang B et al. , Wearable aptamer-field-effect transistor sensing system for noninvasive cortisol monitoring. Sci Adv 8, eabk0967 (2022). [PubMed: 34985954]
28. Choi M et al. , Light-guiding hydrogels for cell-based sensing and optogenetic synthesis. Nat Photonics 7, 987–994 (2013). [PubMed: 25346777]
29. Della Sala F et al. , Mechanical behavior of bioactive poly(ethylene glycol) diacrylate matrices for biomedical application. Journal of the Mechanical Behavior of Biomedical Materials 110, 103885 (2020). [PubMed: 32957192]
30. Grigoryan B et al. , Multivascular networks and functional intravascular topologies within biocompatible hydrogels. Science 364, 458–464 (2019). [PubMed: 31048486]
31. Bretag AH, Synthetic interstitial fluid for isolated mammalian tissue. Life Sci 8, 319–329 (1969).
32. Yoshikawa AM et al. , A massively parallel screening platform for converting aptamers into molecular switches. Nat Commun 14, 2336 (2023). [PubMed: 37095144]
33. Hagel V, Haraszti T, Boehm H, Diffusion and interaction in PEG-DA hydrogels. Biointerphases 8, 36 (2013). [PubMed: 24706145]
34. Lin S, Sangaj N, Razafiarison T, Zhang C, Varghese S, Influence of physical properties of biomaterials on cellular behavior. Pharm Res 28, 1422–1430 (2011). [PubMed: 21331474]
35. Hariri AA et al. , Modular Aptamer Switches for the Continuous Optical Detection of Small-Molecule Analytes in Complex Media. Adv Mater 36, e2304410 (2024). [PubMed: 37975267]
36. Li J, Mooney DJ, Designing hydrogels for controlled drug delivery. Nat Rev Mater 1, (2016).
37. Kim SH, Lee TH, Conformational Dynamics of Poly(T) Single-Stranded DNA at the Single-Molecule Level. J Phys Chem Lett 12, 4576–4584 (2021). [PubMed: 33970634]
38. Hofmann H et al. , Polymer scaling laws of unfolded and intrinsically disordered proteins quantified with single-molecule spectroscopy. Proc Natl Acad Sci U S A 109, 16155–16160 (2012). [PubMed: 22984159]
39. Zhu L, Qiu J, Sakai E, A high modulus hydrogel obtained from hydrogen bond reconstruction and its application in vibration damper. RSC Adv. 7, 43755–43763 (2017).
40. Frangioni JV, In vivo near-infrared fluorescence imaging. Curr Opin Chem Biol 7, 626–634 (2003). [PubMed: 14580568]

41. Wei JCJ et al. , Allometric scaling of skin thickness, elasticity, viscoelasticity to mass for micro-medical device translation: from mice, rats, rabbits, pigs to humans. Sci Rep 7, 15885 (2017). [PubMed: 29162871]

42. Park JH, Allen MG, Prausnitz MR, Biodegradable polymer microneedles: fabrication, mechanics and transdermal drug delivery. J Control Release 104, 51–66 (2005). [PubMed: 15866334]

43. Jacobi U et al. , Porcine ear skin: an in vitro model for human skin. Skin Res Technol 13, 19–24 (2007). [PubMed: 17250528]

44. Moreno MJ, Ling B, Stanimirovic DB, near-infrared fluorescent optical imaging for CNS drug discovery. Expert Opin Drug Discov 15, 903–915 (2020). [PubMed: 32396023]

45. Koren L et al. , Cortisol and corticosterone independence in cortisol-dominant wildlife. Gen Comp Endocrinol 177, 113–119 (2012). [PubMed: 22449618]

46. Oppert M et al. , Plasma cortisol levels before and during “low-dose” hydrocortisone therapy and their relationship to hemodynamic improvement in patients with septic shock. Intensive Care Med 26, 1747–1755 (2000). [PubMed: 11271081]

47. Thomson AH et al. , Variability in hydrocortisone plasma and saliva pharmacokinetics following intravenous and oral administration to patients with adrenal insufficiency. Clin Endocrinol (Oxf) 66, 789–796 (2007). [PubMed: 17437510]

48. Skrajnar S, Cerne M, Bozic M, Peternel L, Effect of replacement fluids saline, gelofusine, and blood on biochemical and hematological parameters in rats subjected to repeated blood sampling. Med Sci Monit 15, BR293–300 (2009). [PubMed: 19789506]

49. Löscher W, Of Mice and Men: The Inter-individual Variability of the Brain's Response to Drugs. eNeuro 11, (2024).

50. Jung C et al. , Plasma, salivary and urinary cortisol levels following physiological and stress doses of hydrocortisone in normal volunteers. BMC Endocr Disord 14, 91 (2014). [PubMed: 25425285]

51. Thompson IAP et al. , An antibody-based molecular switch for continuous small-molecule biosensing. Sci Adv 9, eadh4978 (2023). [PubMed: 37738337]

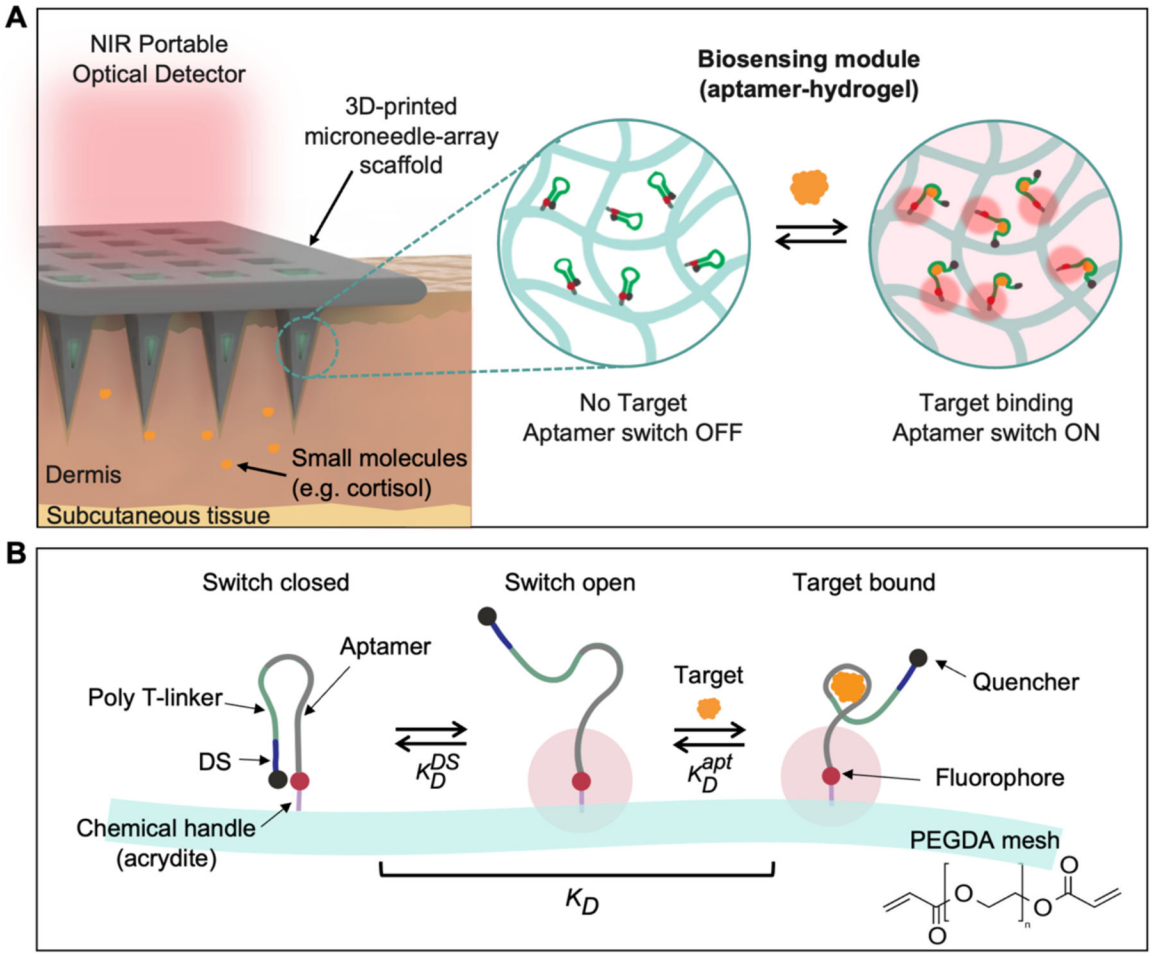

Figure 1. Overview of the microneedle-array biosensor (MAB).

(**A**) Schematic of the MAB, which enables continuous, real-time monitoring of small molecules in dermal ISF. The 3D-printed microneedle-array scaffold ensures effective skin penetration and direct ISF access, such that small molecules can diffuse into the aptamer-hydrogel sensor housed within each microneedle, while the optically opaque scaffold material minimizes background noise from tissue autofluorescence. Each biosensing module consists of aptamer switches functionalized with a fluorophore-quencher pair that are immobilized within the hydrogel mesh. Target binding induces a conformational change in the aptamer, leading to increased fluorescence. A custom-developed portable optical detector (POD) measures the fluorescence intensity through the back openings of the patch. (**B**) The aptamer switches incorporate a poly-T linker with a displacement strand (DS) domain that is complementary to a stretch of aptamer sequence. When the target binds to the aptamer, DS hybridization is disrupted, separating the fluorophore-quencher pair. The resulting fluorescence is proportional to target concentration. The aptamer switches are in turn covalently coupled to a poly(ethylene glycol) diacrylate (PEGDA) hydrogel mesh.

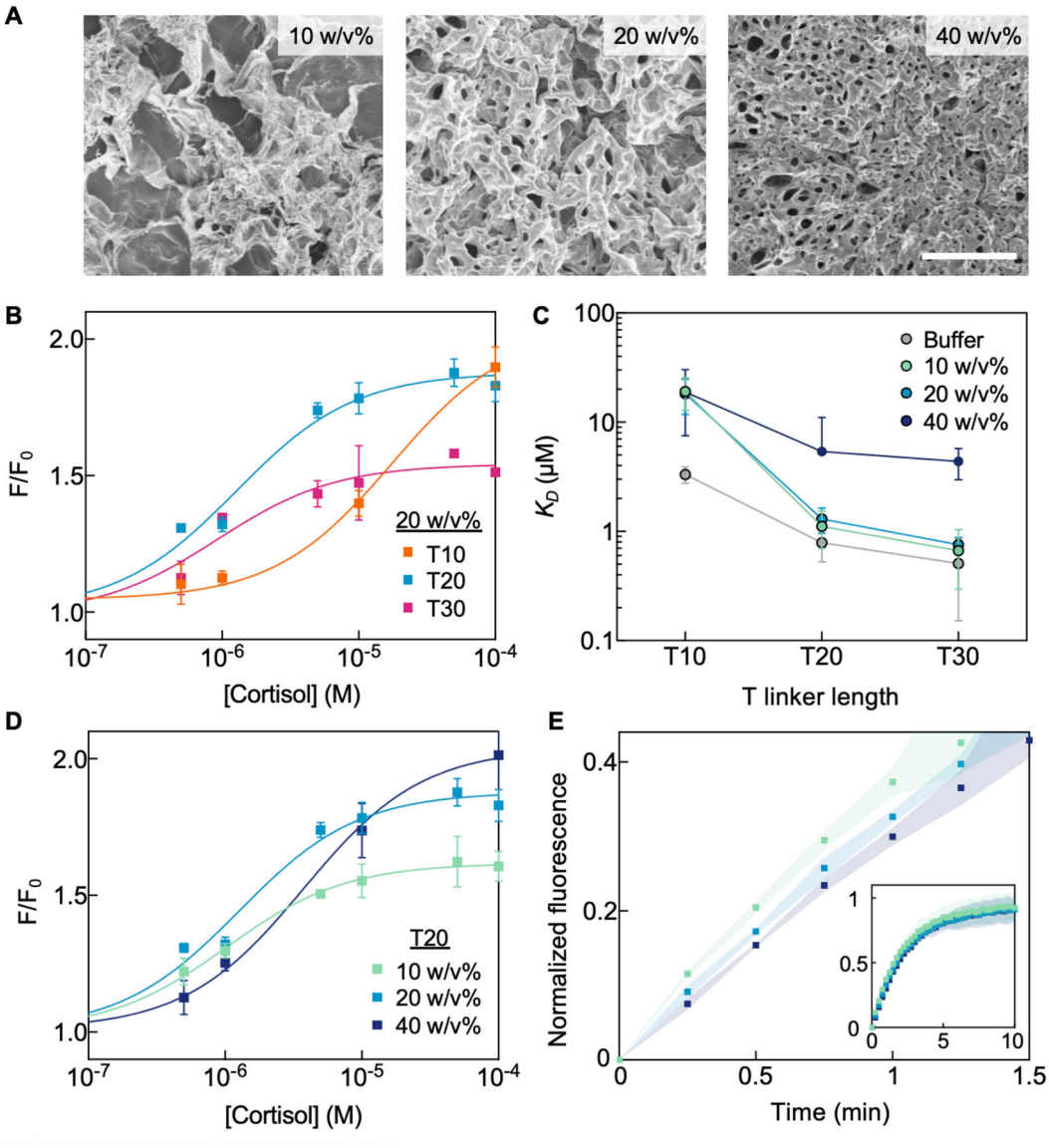

Figure 2. Characterization of cortisol aptamer-hydrogels of varying mesh.

(A) Representative scanning electron microscopy (SEM) images of the hydrogel meshes (10, 20, and 40 w/v%). Scale bar = 50 μm. (**B**) Fluorescence measurements (F/F0) of cortisol aptamer switches with three different poly-T linker lengths (T10, T20, T30) in the 20 w/v% hydrogel mesh. (**C**) *KD* of cortisol switches in buffer versus aptamer-hydrogel modules of varying poly-T linker length and mesh size. (**D**) Fluorescence measurements (F/F0) of the T20 cortisol switch in 10, 20, or 40 w/v% hydrogel meshes. (**E**) Time-dependent fluorescence measurements after spiking 5 μM cortisol onto the T20 cortisol switch immobilized within 10, 20, or 40 w/v% hydrogels. Error bars represent the standard deviation of the average (n = 3). Data fits and normalization are explained in the Experimental Section.

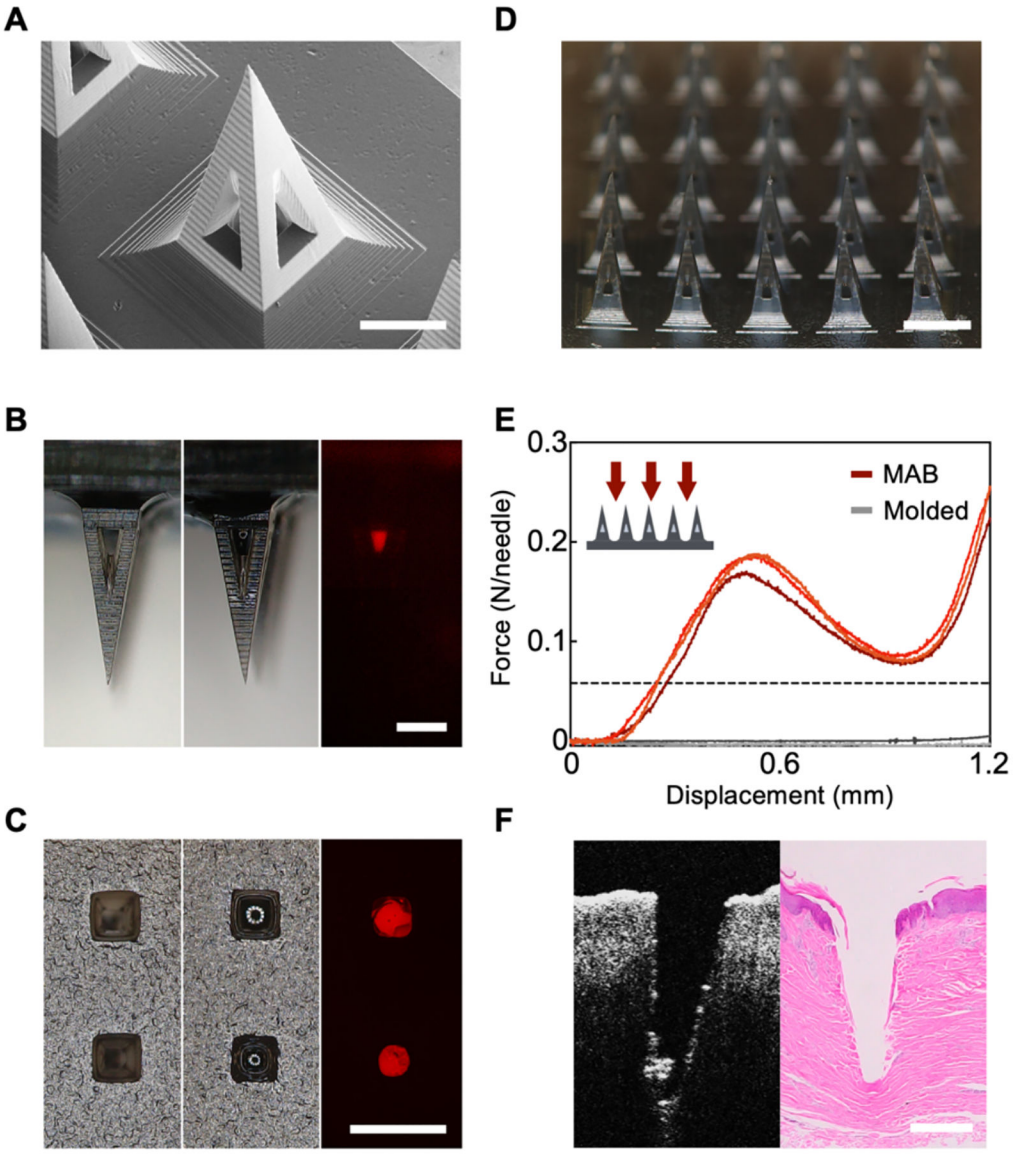

Figure 3. Design and characterization of the MAB scaffold.

(**A**) A scanning electron microscopy (SEM) image of an empty 3D-printed scaffold. Scale bar = 0.5 mm. (**B, C**) Microscopic images of an empty 3D-printed scaffold (left), a 3D-printed scaffold with Cy5-conjugated hydrogel using the brightfield channel (middle), and the corresponding scaffold using the fluorescence channel (right). Scale bar = 0.5 mm. **B**, side view, **C**, bottom view. (**D**) Microscopic image of a 3D-printed scaffold, highlighting the void for the biosensing module. Scale bar = 1 mm. (**E**) Mechanical characterization of our MAB patch (red) and a molded patch of matching hydrogel composition (gray) under a normal compressive load. The fracture force for our MAB exceeds the reported skin puncture force (dashed line), indicating its suitability for skin penetration. (**F**) Optical coherence tomography (left) and hematoxylin and eosin staining (right) of *ex vivo* porcine skin after penetration with a MAB patch. Scale bar = 0.5 mm.

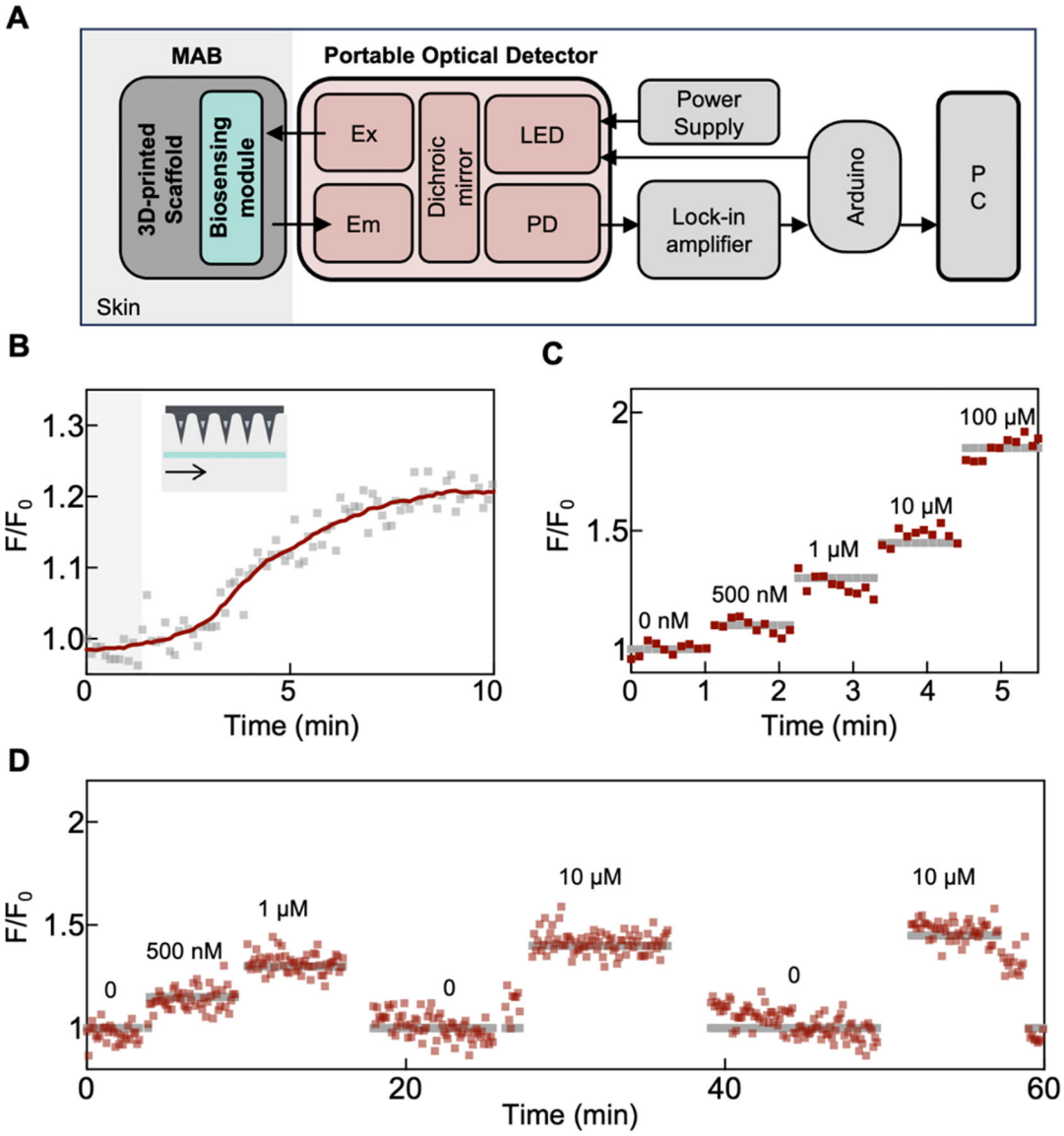

Figure 4. ***In vitro*** **real-time measurement of cortisol using the MAB system.**

(**A**) Block diagram of the full MAB system, including POD. (**B**) Representative temporal response of a MAB patch inserted into a vascularized skin phantom gel that mimics the dermal layer after introducing 500 nM cortisol. (**C**) Representative MAB patch fluorescence as measured through the POD. The patch was inserted into skin phantom gels containing uniform cortisol concentrations. (**D**) Representative continuous measurement of cortisol with a MAB patch serially inserted into various skin phantom gels containing different cortisol concentrations, with wash steps in between.

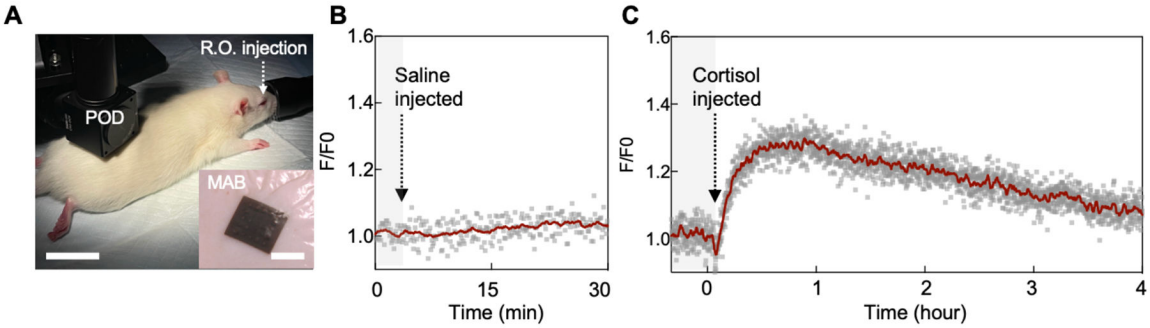

Figure 5. ***In vivo*, continuous measurements of cortisol levels in a rat using the MAB system.** (**A**) Photo of the MAB system inserted into the skin of an anesthetized rat. Scale bar = 3 cm. Inset shows the MAB patch inserted into the shaved skin. Scale bar = 5 mm. (**B**) Representative continuous, real-time measurement from the MAB system after saline injection. (**C**) Representative continuous, real-time measurement of cortisol levels collected from the MAB system after R.O. injection of exogenous cortisol (2.3 mg/kg) at t = 0.